Neutron production in neutron-induced reactions at 96 MeV on ^{56}Fe and ^{208}Pb

I. C. Sagrado García,[1,2,*] J. F. Lecolley,[1] F. R. Lecolley,[1] V. Blideanu,[2] G. Ban,[1] J. M. Fontbonne,[1] G. Itis,[1] J. L. Lecouey,[1] T. Lefort,[1] N. Marie,[1] J. C. Steckmeyer,[1] C. Le Brun,[3] J. Blomgren,[4] C. Johansson,[4] J. Klug,[4] A. Orhn,[4] P. Mermod,[4] N. Olsson,[4] S. Pomp,[4] M. Osterlund,[4] U. Tippawan,[4,5] A. V. Prokofiev,[6] P. Nadel-Turonski,[7] M. Fallot,[8] Y. Foucher,[8] A. Guertin,[8] F. Haddad,[8] and M. Vatre[8]

[1]*Laboratoire de Physique Corpusculaire, ENSICAEN, Université de Caen/Basse Normandie and Centre National de la Recherche Scientifique/IN2P3 Caen, 14050, France*

[2]*Direction des Sciences de la Matière/DAPNIA, Comisariat à l'Energie atomique-Saclay, 91191, France*

[3]*Laboratoire de Physique Subatomique et Cosmologie, Grenoble, 38026, France*

[4]*Department of Neutron Research, Uppsala University, Uppsala, 75120, Sweden*

[5]*Fast Neutron Research Facility, Chiang Mai University, Chiang Mai, 50200, Thailand*

[6]*The Svedberg Laboratory, Uppsala University, Uppsala, 75120, Sweden*

[7]*George Washington University, Washington, D.C. 20052, USA*

[8]*SUBATECH Nantes, 44307, France*

(Received 11 February 2011; revised manuscript received 15 September 2011; published 31 October 2011)

Double-differential cross sections for neutron production were measured in 96-MeV neutron-induced reactions at The Svedberg Laboratory in Uppsala, Sweden. Measurements for Fe and Pb targets were performed using two independent setups: DECOI-DEMON, time-of-flight telescope dedicated to the detection of emitted neutrons with energies between a few and 50 MeV and CLODIA-SCANDAL device devoted to measuring emitted neutrons with energies above 40 MeV. Double-differential cross sections were measured for an angular range between 15 and 98 deg and with low-energy thresholds (≈2 MeV). Angular and energy distributions and total neutron emission cross sections have been obtained from those measurements. Results have been compared with predictions given by different models included in several transport codes (MCNPX, GEANT, TALYS, PHITS, and DYWAN) and with other experimental data (the EXFOR database).

DOI: 10.1103/PhysRevC.84.044619 PACS number(s): 25.40.Fq, 13.75.Cs, 25.40.Sc, 28.20.−v

I. INTRODUCTION

Future accelerator-driven systems (ADS) will couple a high-energy intense proton beam (1 GeV and a few milliamperes) with a spallation target made of heavy elements and a subcritical reactor core. The proton beam impinging on the ADS target will yield a large amount of spallation products, mainly neutrons, protons, and light charged particles, with energies from the mega-electron-volt up to the giga-electron-volt region. Below 30 MeV the nuclear data libraries are nearly complete [1]. Above 200 MeV the cross-section predictions by intranuclear cascade models are in good agreement with the experimental data [2–4]. However, for energies from 30 to 200 MeV there are very few high-quality data, most of them for $(n,xlcp)$ and (p,xn) obtained in the frame of the high- and intermediate-energy nuclear data for accelerator-driven systems (HINDAS) collaboration [1]. Particularly, there is only one nonelastic measurement for (x, xn) reactions [5]. Within this context, the aim of this work, included in the European collaboration EUROTRANS [6] and specifically in the project nuclear data for transmutation (NUDATRA), was to measure (n,xn) double-differential cross sections. Experiments using lead and iron targets were carried out at The Svedberg Laboratory (TSL), Uppsala, Sweden, where a neutron beam at 96 MeV is available. Measurements were accomplished using two independent setups: a DEtector of COIncidence/DEtector MOdular of Neutrons (DECOI-DEMON), time-of-flight telescope dedicated to the detection of emitted neutrons with energies between a few and 50 MeV and a Chamber for LOcalization with DrIft and Amplification/SCAttered Nucleon Detection AssembLy (CLODIA-SCANDAL) device, devoted to measuring emitted neutrons with energies above 40 MeV. Brief descriptions of TSL neutron beam and experimental devices are given in Sec. II. Double-differential cross sections were measured for an angular range between 15 and 98 deg with low-energy thresholds (≈2 MeV). Angular and energy distributions and total neutron emission cross sections have been obtained from double-differential cross sections using the usual methods of analysis. Results are presented in Sec. III. To complete this work several calculations have been accomplished using the main available transport codes (MCNPX, GEANT, TALYS, PHITS, and DYWAN). Comparisons between codes predictions and experimental data are reported in Sec. IV. Moreover, a comparison between (n,xn) and (n, xp) cross sections and a qualitative study of the dependence of (n,xn) cross sections with the incident energy beam and the target mass have been performed using existing experimental data. Results are discussed in Sec. V. The main results and conclusions are summarized in the last section of this document.

II. EXPERIMENTAL SETUP

Two different experiments were performed using the neutron beam available at the TSL laboratory in Uppsala, Sweden. Between the feasibility test realized in 2003 and the

*Present address: Unit of Nuclear Safety Research CIEMAT, 28040, Madrid, Spain.

measurements carried out in 2004, the Uppsala facility was modified in order to increase the neutron flux from 10^5 to 10^6 n/s cm^2. Descriptions of both facilities are given in [7] and [8,9], respectively. Neutrons are produced by ^{7}Li $(p,n)^7Be$ reactions using a 100-MeV proton beam impinging on a lithium target. Emitted neutrons are separated from the primary proton beam using magnetic deflection. Finally, the neutron beam is collimated to reach a diameter of ≈8 cm at the target location. About 50% of neutrons are in a 96-MeV peak; the rest are in a low-energy tail. Events associated with low-energy neutrons were rejected during the data reduction using a technique based on time of flight as detailed in [10]. The beam monitoring is provided by a Faraday cup, where the proton beam is dumped, and a fission detector composed of thin-film breakdown counters [7,11] located in the experimental hall. In order to obtain complete distributions, the measurements were carried out using two independent devices: CLODIA-SCANDAL and DECOI-DEMON. Both devices as well as a detailed description of experimental techniques employed have been presented in [12,13]. In this section only a brief setup description and main steps of the data reduction are reported.

A. CLODIA-SCANDAL

To measure the high-energy neutrons ($T_n > 40$ MeV) a new setup named CLODIA [14] was built at the LPC Caen Laboratory. CLODIA consists of seven neutron-to-proton converters (CH_2) and eight multidrift chambers. The latter are used to measure the recoil proton trajectories and to determine in which converter the interaction occurred. A plastic scintillator was placed in front of CLODIA in order to reject the charged particles emitted from the target. Beside, a SCANDAL arm [15] was used to measure the energy of the recoil proton. The neutron energy is obtained using the angle of the backward elastic neutron-proton scattering and the recoil proton energy. The energy detection threshold ($T_n > 40$ MeV) is due to the energy needed by the recoil proton to arrive into the SCANDAL detector.

B. DECOI-DEMON

To measure the low-energy neutrons ($T_n < 50$ MeV) a time-of-flight telescope named DECOI-DEMON was developed. DECOI is a neutron-to-proton converter made of a plastic scintillator brick (NE102, $5 \times 9 \times 15$ cm^3). DEMON [16,17] is a neutron detector made of a cylindrical liquid scintillator (NE213 of 16-cm diameter and 20-cm thickness). In front of a DEMON cell, a 5-mm-thick plastic scintillator was added to reject charged particles. An incoming neutron, weakly deflected in DECOI, is detected and identified using DEMON. The neutron energy is determined using the well-known time-of-flight technique. The upper energy detection limit ($T_n <$ 50 MeV) is due to the flight distance (≈1m) and to the low efficiency of the DECOI-DEMON device for higher energies.

C. Setup efficiency

A major difficulty in experiments involving neutrons is the weak efficiency of the detectors. There are several experimental techniques (for instance detectors based on neutron capture or liquid scintillators), but usually an intermediate reaction is used. The low efficiency is mainly due to the weak cross section of this reaction. In this work we have used the $np \rightarrow pn$ reaction as a *detection reaction*: the recoil proton and the scattered neutron are detected in CLODIA-SCANDAL and DECOI-DEMON devices, respectively. Due to the weak value of this cross section ($\sigma \approx 15$ mb/sr at 180 deg in the center of mass), experimental efficiency measurements request too much beam time. Therefore, efficiencies have been calculated using simulations. The efficiency of both devices and a detailed description of methods used to obtain it can be found in [12,13]. In this paper, only main results are presented.

1. CLODIA-SCANDAL

The efficiency of the CLODIA-SCANDAL setup is given by the convolution of two main effects: the cross section of the conversion reaction $np \rightarrow pn$ and the geometric conditions. GEANT [18] is a well-suited tool to simulate complex geometries and $np \rightarrow pn$ cross sections are well known [19]. Hence, CLODIA-SCANDAL efficiency has been calculated using GEANT simulations. This efficiency depends on the emitted neutron energy. For instance, for a neutron of 60 MeV the detection efficiency is about 0.1%.

2. DECOI-DEMON

The efficiency of the DECOI-DEMON setup is given by the convolution of three main effects: the cross section of the scattering reaction $np \rightarrow pn'$ in DECOI, the intrinsic efficiency of the DEMON detector, and the geometric conditions. Experimental efficiency of the DECOI-DEMON assembly is not available, however the DEMON efficiency has been already measured [20–22]. GEANT simulations are not able to reproduce the DEMON efficiency since they do not take into account the luminous response of the liquid scintillator. Therefore GEANT is not a well-adapted tool to compute the efficiency of the DECOI-DEMON device. Thus, a specific simulation tool has been developed to calculate this efficiency. To consider the multiple scattering and the luminous response of the DEMON liquid scintillator a recursive algorithm has been used. This method has been validated since the experimental efficiency of a DEMON detector is well reproduced. The DECOI-DEMON efficiency is typically one order of magnitude smaller than that of CLODIA-SCANDAL.

D. Experimental measurements

In order to obtain complete distributions, measurements should be performed at the same angles with both devices. Due to beam time limitations, several measurements were carried out simultaneously. Therefore, the size of different devices and the characteristic of experimental room made it impossible to accomplish the measurements exactly at the same angles; nevertheless, measurements have been performed minimizing the angular differences. Experimental measurements are listed in Table I.

TABLE I. Angles of the emitted neutrons investigated in this work.

Device	Target	Measured angles
CLODIA-SCANDAL	Iron	15, 30, 50, and 70
CLODIA-SCANDAL	Lead	15, 30, 50, and 70
DECOI-DEMON	Iron	15, 24, 55, and 98
DECOI-DEMON	Lead	15, 24, 60, and 98

III. EXPERIMENTAL RESULTS

The analysis techniques described above allow us to determine the energy spectra of emitted neutrons. At this stage the number of emitted neutrons for a given energy and angle, $N(\theta, T_n)$, is known. Double-differential cross sections have been extracted directly from $N(\theta, T_n)$. Other important observables as energy and angular distributions have been derived from double-differential cross sections using common techniques. Finally, total neutron emission cross sections have been calculated from angular and energy distributions.

A. Double-differential cross section

Double-differential cross sections have been obtained from $N(\theta, T_n)$ using the nonrelativistic expression

$$\frac{d^2\sigma(\theta, T_n)}{d\Omega\, dT_n} = \frac{1}{\Delta T_n \Delta\Omega\, n_c} \frac{N(\theta, T_n)}{\epsilon(T_n)\, \Phi} \ (\times 10^{27}\ \text{mb/sr}), \quad (1)$$

where ΔT_n is the energy step in MeV. In this case $\Delta T_n = 4$ MeV mainly due to the resolution of detection devices. $\Delta\Omega$ is the solid angle detector in sr. To take into account the target geometry and the characteristics of two experimental devices the solid angle has been calculated for each case by simulation using GEANT [18]. n_c is the number of target nuclei per cm^2. This value is easily determined from the dimensions and the density of the target. $N(\theta, T_n)$ is the number of detected neutrons for a given energy T_n at a given angle θ. $\epsilon(T_n)$ is the device efficiency. Φ is the number of neutrons incident on the target. Φ has been obtained from the neutron flux given by the monitors and the beam diameter at the target position ($S = 8$ cm).

Figures 1 and 2 show the double-differential distributions for lead and iron targets for an angular range from 15 to 100 deg and with an energy threshold of $\approx$2 MeV. Distributions for $T_n > 40$ MeV have been obtained from CLODIA-SCANDAL collected data and distributions for $T_n < 50$ MeV have been extracted from DECOI-DEMON measurements. At 15 deg, the two sets of measurements match well, with differences around 10% in the overlapping region, for both lead and iron targets. Discrepancies correspond essentially to experimental systematic uncertainties [12,13]. For distributions measured at 24–30, 50–60, and 50–55 deg the two measurements agree, since, due to the experimental resolution, the angular difference is not significant. Distributions at 70 and 98 deg are directly CLODIA-SCANDAL and DECOI-DEMON measurements, respectively. Measured spectra are characterized by three different components: a elastic peak at the beam energy, a pre-equilibrium region, and a low-energy peak characteristic for the evaporation process. Elastic and

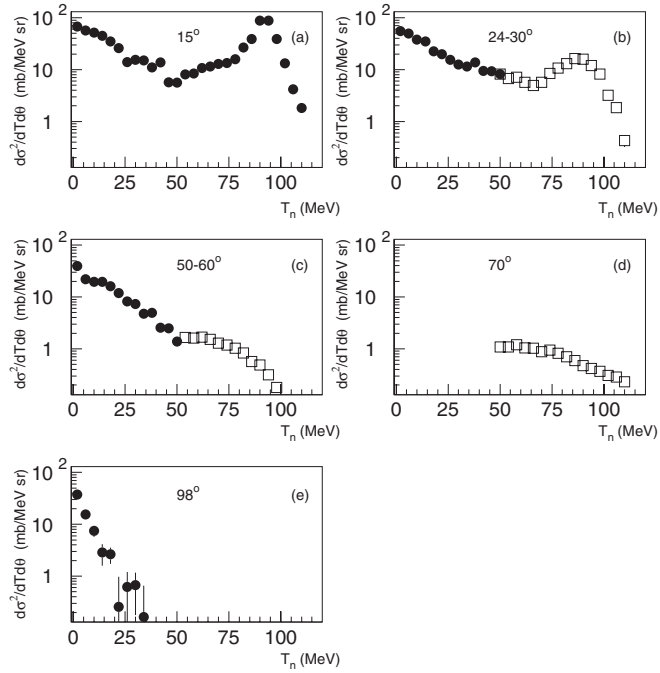

FIG. 1. (n,xn) measured double-differential cross sections at 96 MeV for lead at different angles: (a) 15°. (b) 30° (squares) and 24° (circles). (c) 50° (squares) and 60° (circles). (d) 70°. (e) 98°.

pre-equilibrium contributions exhibit a strong dependence on angle, whereas the evaporation component presents an isotropic behavior.

Although this work is focused on nonelastic emissions, elastic cross sections have been calculated in order to validate analysis and normalization procedures. Concerning CLODIA-

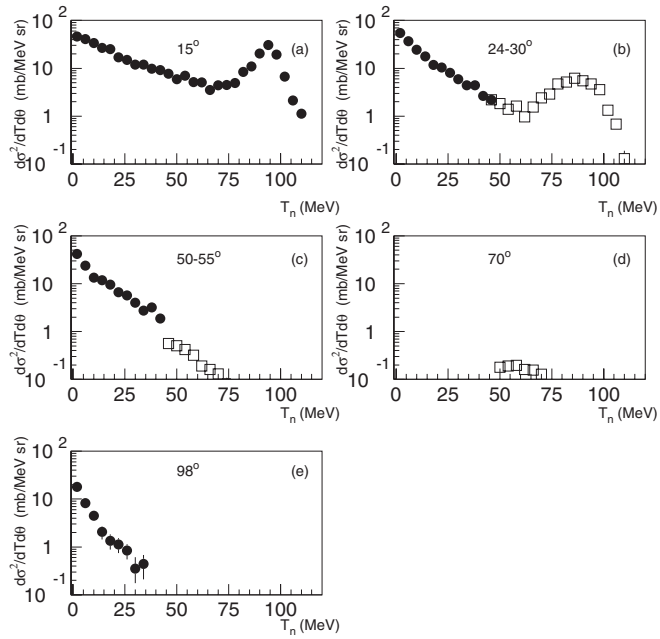

FIG. 2. (n,xn) measured double-differential cross sections at 96 MeV for iron at different angles: (a) 15°. (b) 30° (squares) and 24° (circles). (c) 50° (squares) and 55° (circles). (d) 70°. (e) 98°.

TABLE II. Measured elastic cross sections for lead and iron using CLODIA-SCANDAL and DECOI-DEMON devices.

Angle	Lead (mb/sr)	Iron (mb/sr)
15°	993 ± 20	380 ± 4
24°	364 ± 4	38 ± 1
30°	212 ± 32	75 ± 11
60°	2.8 ± 1	1.9 ± 1

SCANDAL, elastic cross sections have been calculated from double-differential cross sections integrating over the elastic peak. Note that this technique is only valid for small angles (15 and 30 deg). The DECOI-DEMON device allows us to measure elastic cross sections at any angle. Both neutrons and protons may interact in a DEMON liquid scintillator; since the DECOI-DEMON device is devoted to measuring neutrons, a plastic scintillator is placed in front of the DEMON module to reject charged particles. Nevertheless, one can use the plastic scintillator to identify protons. High-energy neutrons coming from elastic reactions into the target arrive into the DECOI converter. These neutrons can produce high-energy protons scattered at a small angle. These protons are detected first in the plastic scintillator and then in the DEMON detector. Therefore the high-energy protons counted in the plastic scintillator allow to measure the elastic cross section. The elastic cross sections obtained in the present work are summarized in Table II. They are in good agreement with previous experimental measurements [15,23–25] for both lead and iron. This fact points out the reliability of the normalization procedure.

B. Angular distributions

Angular distributions have been obtained from double-differential distributions. For the sake of clarity, the elastic peak is not considered. Once the elastic contribution (approximated by a Gaussian) is rejected, the resulting spectrum is integrated from the energy threshold ($T_t = 4 \pm 2$ MeV) to the energy beam ($T_b = 96$ MeV):

$$\frac{d\sigma}{d\Omega} = \int_{T_t}^{T_b} \left(\frac{d^2\sigma}{dT_n d\Omega} \right) (\theta, T_n)\ dT_n. \qquad (2)$$

The resulting values (Table III and Fig. 3) decrease strongly with the angle, keeping the same behavior as double-differential distributions.

TABLE III. (n,xn) experimental angular cross sections obtained for lead and iron targets at 96 MeV.

Angle	Lead (mb/sr)	Iron (mb/sr)
15°	1982 ± 83	1221 ± 47
30°	1317 ± 76	818 ± 34
50°	717 ± 66	561 ± 39
70°	507 ± 88	363 ± 50
98°	259 ± 23	159 ± 11

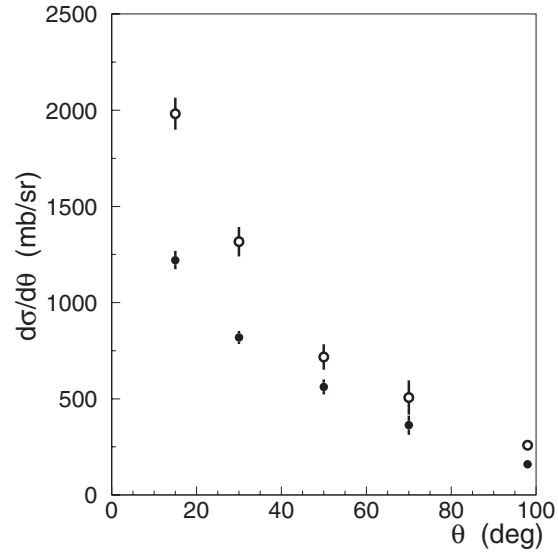

FIG. 3. (n,xn) angular distributions for lead (open circles) and iron (solid circles) at 96 MeV.

C. Energy distributions

Energy distributions can be calculated from double-differential cross sections using the Kalbach parametrization [26]. This technique has been successfully used to obtain energy distributions in $(n,xlcp)$ and (p,xn) reactions [10,27,28]. A double-differential cross section can be expressed as a function of the energy differential cross section:

$$\frac{d^2\sigma}{d\Omega dT} = \left(\frac{1}{4\pi} \frac{d\sigma}{dT} \frac{a}{\sinh(a)} \right) \times [\cosh(a\ \cos\theta) + f_{\mathrm{MSD}}\ \sinh(a\ \cos\theta)], \qquad (3)$$

where a depends on the characteristics of the projectile and of the emitted particle and f_{MSD} is the fraction of the nonequilibrium emission (if $f_{\mathrm{MSD}} = 1$ there is no equilibrium

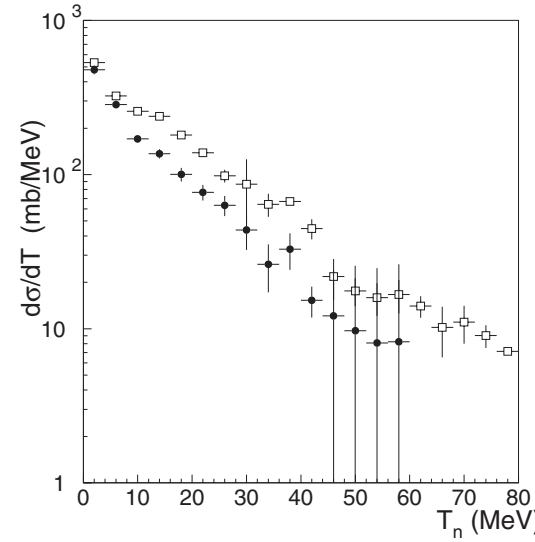

FIG. 4. (n,xn) energy distributions for lead (open symbols) and iron (solid symbols). See text for details.

TABLE IV. (n,xn) total neutron emission cross section at 96 MeV.

Target	$\int dT$ (mb)	$\int d\Omega$ (mb)
Lead	8663	6132
Iron	5868	4304

emission). For the sake of clarity we have removed the elastic contribution to calculate energy distributions. Results are shown in Fig. 4. Energy distributions have the same behavior for lead and iron. An important contribution at low energy due to the evaporation process is observed since neutrons are not affected by the Coulomb barrier. As expected, energy cross sections for lead are higher than for iron; the ratio is essentially constant over the whole energy range.

D. Total neutron emission cross sections

Total neutron emission cross sections have been calculated from energy and angular distributions (Table IV). Values extracted from energy distributions could be overestimated since energy distributions are dominated by the low-energy points which have been measured at the detection limit. Moreover, energy distributions have been calculated using the Kalbach parametrization and it is not easy to evaluate the uncertainties associated with this technique.

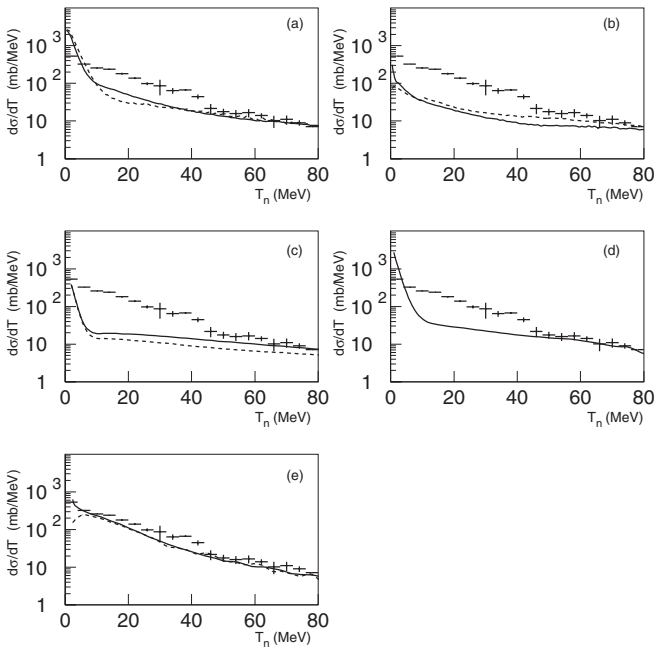

FIG. 5. Comparison between experimental and calculated energy differential cross sections for Pb (n, xn) reaction at 96 MeV using different available codes and models: (a) MCNPX with GNASH (continuous line) and INCL4-ABLA (dashed line). (b) GEANT3 with GHEISA (continuous line) and FLUKA (dashed line). (c) DYWAN with (continuous) and without (dashed line) symmetry energy term. (d) TALYS. (e) PHITS with QMD and SDM (continuous line) and with QMD without evaporation model (dashed line).

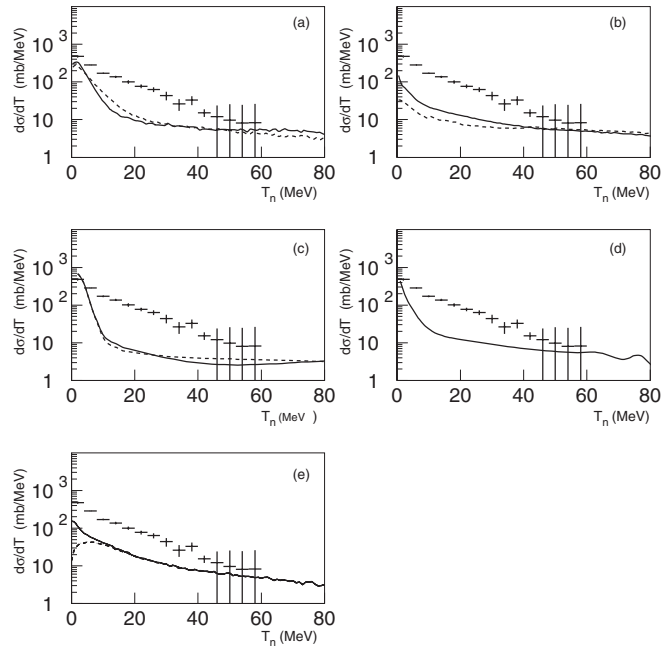

FIG. 6. Comparison between experimental and calculated energy differential cross sections for Fe (n, xn) reactions at 96 MeV using different available codes and models: (a) MCNPX with GNASH (continuous line) and INCL4-ABLA (dashed line). (b) GEANT3 with GHEISA (continuous line) and FLUKA (dashed line). (c) DYWAN with (continuous) and without (dashed line) symmetry energy term. (d) TALYS. (e) PHITS with QMD and SDM (continuous line) and with QMD without evaporation model (dashed line).

IV. THEORETICAL CALCULATIONS

Monte Carlo transport codes are usually employed for design and decommissioning of nuclear facilities. A good prediction of neutron emission is particularly important in reactor and radio-protection studies. Therefore the validation of codes' and models' performances is essential. In this section, (n,xn) energy distributions for lead and iron have been calculated with commonly used transport codes: MCNPX [29] with GNASH [30] and INCL4-ABLA [3,31], GEANT3 with GHEISA [18] and FLUKA [32], TALYS [33], PHITS [34] with QMD and SDM [35], and DYWAN [36], an original microscopic model able to take or not take into account the symmetry energy term (isospin). Comparisons between codes predictions and experimental data are reported in Figs. 5 and 6. Quantitatively, measurements are systematically underestimated. It is worth noting that the PHITS prediction computed using QMD and SDM models agrees fairly well with measurements in the whole energy range. Qualitatively, only the PHITS simulation is able to reproduce the shape of measured distributions. The other calculations reproduce the experimental trend only for energies higher than 50 MeV. Moreover, around 10 MeV, they present an abrupt transition between the evaporation peak and a flat pre-equilibrium contribution which is not observed experimentally. In order to analyze this point, the comparison between measurements performed at 98 deg, where evaporation dominates, and data from the ENDF/B-VII.0 evaluated library is reported in Fig. 7.

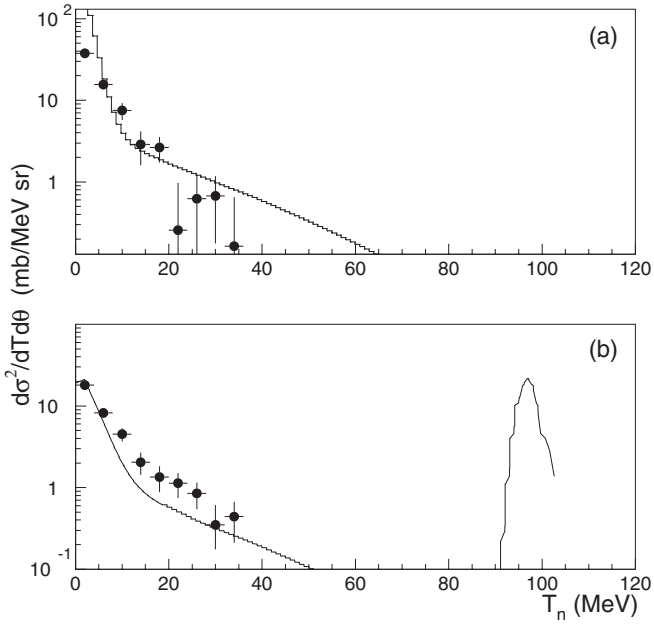

FIG. 7. Double-differential cross sections for (a) lead and (b) iron at 98°. Experimental data (symbols) vs ENDF/B-VII.0 evaluated library (line).

Evaluated and experimental data behave alike and, considering the experimental uncertainties, a reasonable agreement is found. This fact points out that calculations are able to compute each separated contribution, but they have difficulties reproducing the experimental measurements in the region where evaporation and pre-equilibrium are not isolated and both processes contribute to the emission of neutrons.

V. CROSS-SECTION ANALYSIS IN THE EXPERIMENTAL FRAMEWORK

To complete this work several experimental data available in the EXFOR database [37] have been used. Comparisons between (n,xn) and (n,xp) energy distributions at 96 MeV are reported in Fig. 8. (n,xn) cross sections are higher than (n,xp) ones in the whole energy range. At low energy, where the evaporation process dominates, this is due to the fact that neutrons are not affected by the Coulomb barrier. In the pre-equilibrium region the difference is caused by the isospin asymmetry, as has been extensively studied in [38] and [39].

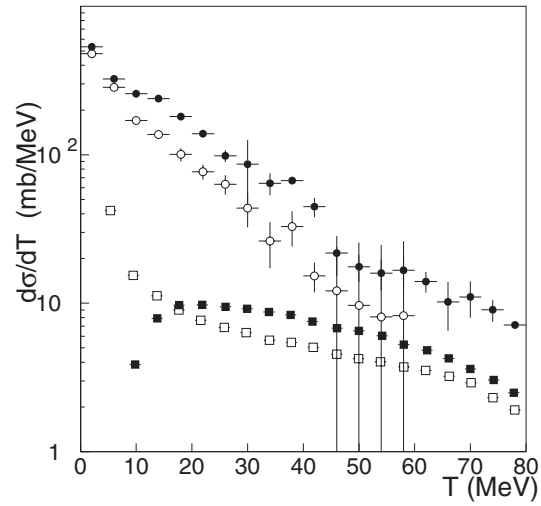

FIG. 8. (n,xn) and (n,xp) energy distributions at 96 MeV for lead and iron targets: Pb (n,xn) (solid circles), Pb (n,xp) (solid squares), Fe (n,xn) (open circles), and Fe (n,xp) (open squares). Data are from present work and from [10].

Concerning (n,xn) data, the EXFOR database [37] contains few experimental data, most of them measured with low-energy beams ($T_b < 26$ MeV). At intermediate energies ($30 < T_b < 200$ MeV) only one measurement exists [5] (Table V). Available double-differential cross sections measured at $\theta \sim 20°$–$30°$ for several beam energies on lead (or bismuth) and iron targets are presented in Fig. 9. In the intermediate-energy region, associated with the pre-equilibrium emission, double-differential cross sections are not very sensitive to the beam energy and the values measured using low-energy beams are comparable to those obtained in this work. Unfortunately, there are no data of energy distributions with incident neutron beams between $26 < T_b < 96$ MeV. Thus, a quantitative analysis using low-energy data has been performed. To get a quantitative estimation of the pre-equilibrium contribution, a partial pre-equilibrium cross section σ has been derived from the differential cross section:

$$\sigma = \int_{T_n > T_t} \frac{d\sigma}{dT_n}\, dT_n \quad (T_t = 12\,\text{MeV}). \tag{4}$$

The energy threshold T_t is chosen to allow the use of all available data (up to $T_b = 18$ MeV). The results obtained are represented as a function of the target mass in Fig. 10(a). Values from this work are larger than the others. However,

TABLE V. Available EXFOR data for (n,xn) reactions at intermediate energies $15 < T_b < 200$ MeV.

Beam energy (T_b)	Targets	Quantity	Angular range	Energy threshold	Ref.
65 MeV	Fe, Sn, Pb	$\frac{d^2\sigma}{dTd\Omega}$	9.5°–24°	20 MeV	[5]
26 MeV	V, Fe, Cu, Nb, W, Bi	$\frac{d^2\sigma}{dTd\Omega}$, $\frac{d\sigma}{dT}$	25°–145°	12 MeV	[40]
20 MeV	Nb, Ho, Ta, Bi	$\frac{d^2\sigma}{dTd\Omega}$, $\frac{d\sigma}{dT}$	15°–154°	2.5 MeV	[41]
18 MeV	Al, Fe, Ni, Zr, Nb, Cu, Bi, Th, U	$\frac{d^2\sigma}{dTd\Omega}$, $\frac{d\sigma}{dT}$	30°–150°	1 MeV	[42–44]

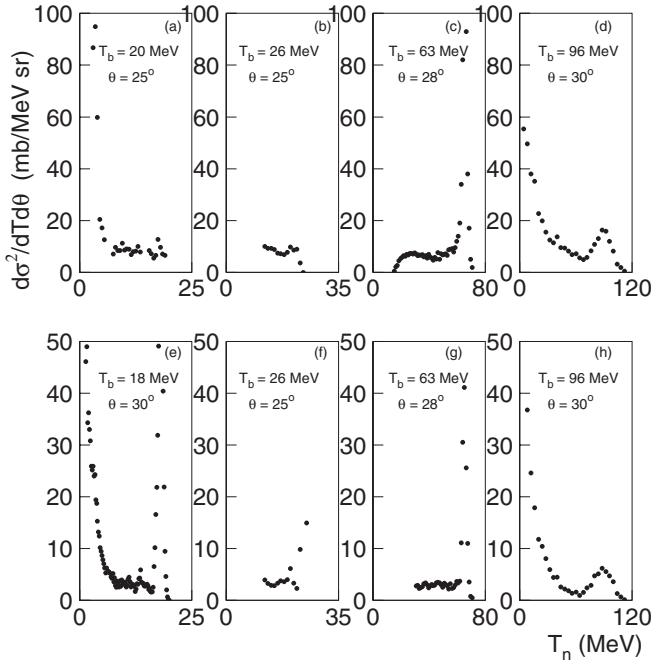

FIG. 9. (n,xn) double-differential cross sections for (a) and (b) bismuth, (c) and (d) lead, and (e)–(h) iron at $\theta \sim 20^\circ$–30° for several beam energies. Data are from this work and from [5,40–42,44].

it is worth noting that there is a difference of more than 70 MeV in the incident beam energy. To obtain a comparable quantity the partial pre-equilibrium cross section per incident mega-electron-volt has been calculated:

$$\frac{\sigma}{T_b - T_t}. \tag{5}$$

The results are shown in Fig. 10(b). The good agreement between our data and the others points out the reliability of data reduction and normalization procedures used in this work. Moreover, a strong correlation is observed between the production ratio per mega-electron-volt and the target mass. The energy beam dependence of the (n,xn) and (n,xp) partial cross sections for targets around $Z = 82$ (Pb and Bi) and $Z = 26$ (Fe, Cu, and Co) are shown in Fig. 11. The data distributions could be consistent with a linear dependence. Nevertheless, due to lack of data between 30 and 90 MeV, this point could not be verified.

VI. SUMMARY

Double-differential cross sections for neutron production have been measured in 96-MeV neutron-induced reactions on lead and iron targets. Experimental data have been measured for an angular range between 15 and 98 deg with energy thresholds of ≈2 MeV. However, due to the difficulties inherent to this kind of experiment (background, detection efficiencies, neutron monitoring, etc.), the results are obtained with significant uncertainties. Strong angle dependence is observed for elastic and pre-equilibrium contributions, whereas the evaporation component remains isotropic. Angular differential cross sections have been calculated from measured data. They decrease strongly with the angle, keeping the same behavior

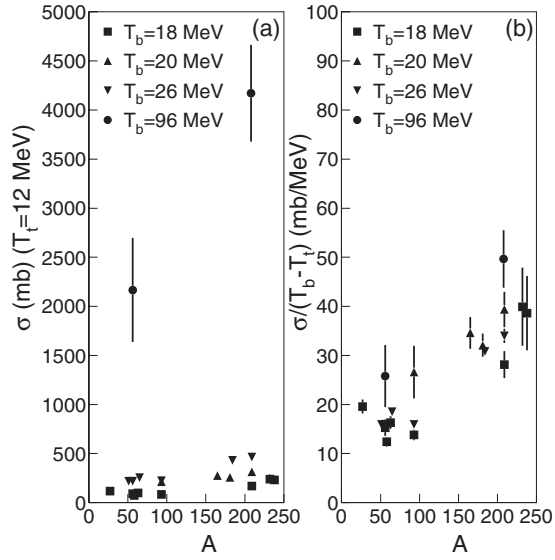

FIG. 10. (n,xn) evaluated (a) partial pre-equilibrium cross section σ and (b) partial pre-equilibrium cross section per incident MeV for several targets. Data are from this work and from [40–44].

of double-differential distributions. Energy distributions have been also obtained from experimental data using the Kalbach systematics. An important contribution is observed at low energy since neutrons are not affected by the Coulomb barrier. Total neutron emission cross sections have been calculated from angular and energy distributions, however the data extracted from energy distributions could be overestimated. Energy distributions for measured reactions have been compared with transport codes predictions. Quantitatively,

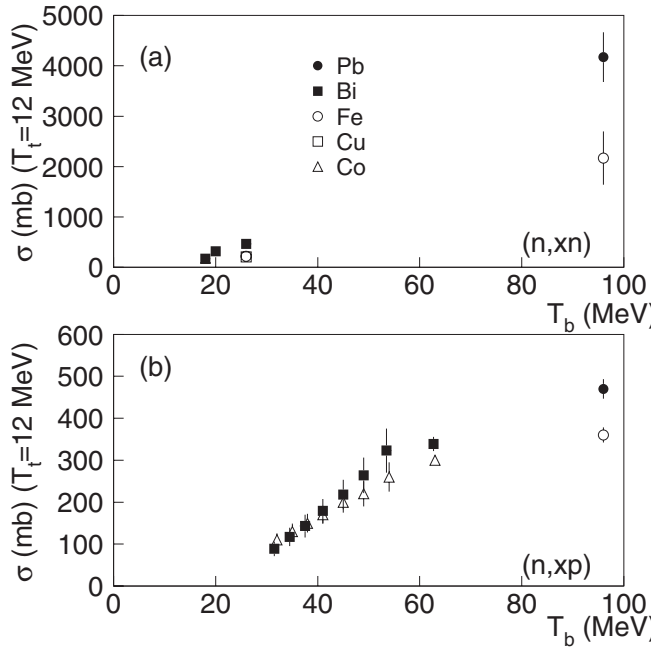

FIG. 11. Energy dependence of the evaluated partial pre-equilibrium cross section for (a) (n,xn) and (b) (n,xp) reactions for several targets. Data are from this work and from [10,40,41,44–46].

experimental data are systematically underestimated, although we have to keep in mind the important uncertainties associated with experimental data. Qualitatively, only PHITS predictions are able to reproduce the experimental shape. The other codes follow the experimental trend only for energies higher than 50 MeV and predict an abrupt transition between evaporation and the pre-equilibrium process, which is not observed experimentally. Comparison between the results obtained in this work and existing experimental data shows that, due to the isospin asymmetry, (n,xn) pre-equilibrium emissions are higher than (n,xp) ones. Moreover, (n,xn) double-differential cross sections associated with pre-equilibrium emission are not very sensitive to the neutron beam energy while a strong correlation between the production ratio per mega-electron-volt and the target mass is observed. The energy beam dependence of the (n,xn) and (n,xp) partial cross sections could be consistent with a linear dependence. Nevertheless, this point could not be verified due to lack of data.

ACKNOWLEDGMENTS

This work was supported by the European Community under the EUROTRANS project (Contract No. FI6W-CT-2004-516520). We would like to thank the TSL staff for their assistance.

[1] European Community, Contract No. FIKW-CT-2000-0031.
[2] H. W. Bertini, Phys. Rev. **188**, 1711 (1969).
[3] A. Boudard, J. Cugnon, S. Leray, and C. Volant, Phys. Rev. C **66**, 044615 (2002).
[4] H. Kumawat and V. S. Barashenkov, Eur. Phys. J. A **26**, 61 (2005).
[5] E. L. Hjort, F. P. Brady, J. R. Drummond, B. McEachern, J. H. Osborne, J. L. Romero, D. S. Sorenson, and H. H. K. Tang, Phys. Rev. C **53**, 237 (1996).
[6] Contract no. FI6W-CT-2004-516520 (2004).
[7] H. Condé *et al.*, Nucl. Instr. Meth Phys. Res. A **292**, 121 (1990).
[8] L. O. Andersson *et al.*, in Proceedings of EPAC 2004, Lucerne, Switzerland (2004).
[9] S. Pomp *et al.*, in *Proceedings of the International Conference on Nuclear Data for Science and Technology, Santa Fe, New Mexico, USA, Sep. 26-Oct. 1, 2004*, AIP Conf. Proc. No. 769, p. 780 (Melville, New York, 2005).
[10] V. Blideanu *et al.*, Phys. Rev. C **70**, 014607 (2004).
[11] A. Smirnov, V. P. Eismont, and A. V. Prokofiev, Radiat. Meas. **25**, 151 (1995).
[12] G. Ban *et al.*, Nucl. Instr. Meth. A. (submitted for publication).
[13] I. C. Sagrado García, Ph.D. thesis, University of Caen, 2006.
[14] I. C. Sagrado García *et al.*, POS (**FNDA2006**) 009 (2006).
[15] J. Klug *et al.*, Nucl. Instr. Meth. Phys. Res. A **489**, 282 (2002).
[16] S. Mouatassim, Ph.D. thesis. University Louis Pasteur de Strasbourg, 1994.
[17] H. Moustafa, Ph.D. thesis. Université Catholique de Louvain (1993).
[18] GEANT Detector Description and Simulation Tool, CERN Program Library Long Writeup W5013.
[19] J. Binstock, Phys. Rev. C **10**, 19 (1974).
[20] F. R. Lecolley, Ph.D. thesis. University of Caen, 1996.
[21] J. Thun *et al.*, Nucl. Instr. Meth. A **478**, 559 (2002).
[22] I. Tilquin *et al.*, Nucl. Instr. Meth. A **365**, 446 (1995).
[23] G. L. Salmom, Nucl. Phys. **21**, 15 (1960).
[24] A. Ohrn *et al.*, Phys. Rev. C **77**, 024605 (2008).
[25] J. H. Osborne *et al.*, Phys. Rev. C **70**, 054613 (2004).
[26] C. Kalbach, Phys. Rev. C **37**, 2350 (1988).
[27] A. Guertin *et al.*, Eur. Phys. J. A **23**, 49 (2005).
[28] M. Kerveno *et al.*, Phys. Rev. C **66**, 014601 (2002).
[29] D. B. Pelowitz (ed.), MCNPX User's Manual Version 2.5.0, LA-CP-05-0369, LANL (2005).
[30] M. B. Chadwick *et al.*, LA-UR-98-1825. LANL, Los Alamos, New Mexico (1998).
[31] A. R. Junghans, M. de Jong, H. G. Clerc, A. V. Ignatyuk, G. A. Kudyaev, and K. H. Schmidt, Nucl. Phys. A **629**, 635 (1998).
[32] A. Fasso, A. Ferrari, J. Ranft, and P. R. Sala, in Proceedings of the Fourth International Conference on Calorimetry in High Energy Physics, La Biodola, Italy (1993).
[33] A. J. Koning, S. Hilaire, and M. Duijvestijn, NRG Report No. 21297/04.62741/P FAI/AK/AK (2004).
[34] H. Iwase, K. Niita, and T. Nakamura, J. Nucl. Sci. Technol. **39**, 1142 (2002).
[35] K. Niita, S. Chiba, T. Maruyama, T. Maruyama, H. Takada, T. Fukahori, Y. Nakahara, and A. Iwamoto, Phys. Rev. C **52**, 2620 (1995).
[36] B. Jouault, F. Sébille, and V. de la Mota, Nucl. Phys. A **628**, 119 (1998).
[37] EXFOR database [http://www.nea.fr/html/dbdata/x4/].
[38] F. Sebille, V. de la Mota, I. C. Sagrado García, J. F. Lecolley, and V. Blideanu, Phys. Rev. C **76**, 024603 (2007).
[39] F. Sebille, V. de la Mota, I. C. Sagrado García, J. F. Lecolley, and V. Blideanu, Nucl. Phys. A **791**, 313 (2007).
[40] A. Marcinkowski, R. W. Finlay, G. Randers-Pehrson, C. E. Brient, R. Kurup, S. Mellema, A. Meigooni, and R. Taylor, Nucl. Phys. A **402**, 220 (1983).
[41] A. Marcinkowski, J. Rapaport, R. Finlay, X. Aslanoglu, and D. Kielan, Nucl. Phys. A **530**, 75 (1991).
[42] M. Baba, S. Matsuayama, T. Ito, T. Ohkubo, and N. Hirakawa, J. Nucl. Sci. Tech. **31**, 757 (1994).
[43] M. Baba, H. Wakabayashi, N. Ito, K. Maeda, and N. Hirakawa, J. Nucl. Sci. Tech. **27**, 601 (1990).
[44] M. Baba, M. Ishikawa, N. Yabuta, T. Kikuchi, H. Wakabayashi, and N. Hirakawa, in *Proceedings of the International Conference on Nuclear Data for Science and Technology, Mito, Japan, 1988*, edited by S. Igarasi (Japan Atomic Energy Research Institute, Tokai-mura, 1988), p. 291.
[45] N. Nica, S. Benck, E. Raeymackers, I. Slypen, J. P. Meulders, and V. Corcalciuc, Nucl. Part. Phys. **28**, 2823 (2002).
[46] E. Raeymackers, S. Benck, N. Nica, I. Slypen, J. P. Meulders, V. Corcalciuc, and A. J. Koning, Nucl. Phys. A **726**, 210 (2003).